PAPER

Cite this: *RSC Adv.*, 2019, **9**, 15323

Crystal structure, hydrogen bonding, mechanical properties and Raman spectrum of the lead uranyl silicate monohydrate mineral kasolite†

Francisco Colmenero, [ID] *[a] Jakub Plášil, [ID] [b] Joaquín Cobos, [ID] [c] Jiří Sejkora, [ID] [d] Vicente Timón, [ID] [a] Jiří Čejka [ID] [d] and Laura J. Bonales [ID] [c]

The crystal structure, hydrogen bonding, mechanical properties and Raman spectrum of the lead uranyl silicate monohydrate mineral kasolite, $Pb(UO_2)(SiO_4) \cdot H_2O$, are investigated by means of first-principles solid-state methods based on density functional theory using plane waves and pseudopotentials. The computed unit cell parameters, bond lengths and angles and X-ray powder pattern of kasolite are found to be in very good agreement with their experimental counterparts. The calculated hydrogen atom positions and associated hydrogen bond structure in the unit cell of kasolite confirmed the hydrogen bond scheme previously determined from X-ray diffraction data. The kasolite crystal structure is formed from uranyl silicate layers having the uranophane sheet anion-topology. The lead ions and water molecules are located in the interlayer space. Water molecules belong to the coordination structure of lead interlayer ions and reinforce the structure by hydrogen bonding between the uranyl silicate sheets. The hydrogen bonding in kasolite is strong and dual, that is, the water molecules are distributed in pairs, held together by two symmetrically related hydrogen bonds, one being directed from the first water molecule to the second one and the other from the second water molecule to the first one. As a result of the full structure determination of kasolite, the determination of its mechanical properties and Raman spectrum becomes possible using theoretical methods. The mechanical properties and mechanical stability of the structure of kasolite are studied using the finite deformation technique. The bulk modulus and its pressure derivatives, the Young and shear moduli, the Poisson ratio and the ductility, hardness and anisotropy indices are reported. Kasolite is a hard and brittle mineral possessing a large bulk modulus of the order of $B \sim 71$ GPa. The structure is mechanically stable and very isotropic. The large mechanical isotropy of the structure is unexpected since layered structures are commonly very anisotropic and results from the strong dual hydrogen bonding among the uranyl silicate sheets. The experimental Raman spectrum of kasolite is recorded from a natural mineral sample from the Jánská vein, Příbram base metal ore district, Czech Republic, and determined by using density functional perturbation theory. The agreement is excellent and, therefore, the theoretical calculations are employed to assign the experimental spectrum. Besides, the theoretical results are used to guide the resolution into single components of the bands from the experimental spectrum. A large number of kasolite Raman bands are reassigned. Three bands of the experimental spectrum located at the wavenumbers 1015, 977 and 813 cm^{-1}, are identified as combination bands.

[a]*Instituto de Estructura de la Materia (IEM-CSIC), C/ Serrano, 113, 28006 Madrid, Spain. E-mail: francisco.colmenero@iem.cfmac.csic.es*

[b]*Institute of Physics ASCR, v.v.i., Na Slovance 2, 182 21, Praha 8, Czech Republic*

[c]*Centro de Investigaciones Energéticas, Medioambientales y Tecnológicas (CIEMAT), Avda/Complutense, 40, 28040 – Madrid, Spain*

[d]*Mineralogicko-Petrologické Oddělení, Národní Muzeum, Cirkusová 1740, 193 00 Praha 9, Czech Republic*

† Electronic supplementary information (ESI) available: Pictures of the atomic motions in the Raman active vibrational modes of kasolite mineral. CCDC 1907046. For ESI and crystallographic data in CIF or other electronic format see DOI: 10.1039/c9ra02931a

1 Introduction

Kasolite, $Pb(UO_2)(SiO_4) \cdot H_2O$, is an important hydrated uranyl silicate mineral phase which was found for the first time by Schoep in 1921.[1] Its name, was coined by Schoep, emphasizing the locality in which it was found for the first time: the Kasolo mine (Katanga, Democratic Republic of the Congo).[1] Uranyl silicates are the most abundant uranyl minerals in the Earth's surface and form predominantly in uranium rich aqueous solutions containing the ubiquitous silicate ion.[2,3] They have been invariably found as a result of the oxidation and dissolution/precipitation processes occurring in uraninite-

bearing ore deposits.[4–8] Kasolite has also been documented to be a fundamental component of the paragenetic sequence of secondary phases that arises from the corrosion of spent nuclear fuel (SNF) under the final geological disposal conditions.[9–13] Kasolite, the only known uranyl silicate containing lead, together with the lead uranyl oxides, such as vandendriesscheite or curite,[14,15] is among the most relevant lead uranyl containing phases. The study of uranyl silicate phases is extremely important because the knowledge of their long-term stability under various environmental conditions is required to understand the complex assemblages of uranyl minerals found at uranium deposits.[2,3] While the crystal structure of kasolite has long been investigated,[16–21] its full structure determination, including the positions of the hydrogen atoms has been reported only recently.[22]

One of the most important sources of lead in uranium containing minerals is *via* uranium radioactive decay.[2,3] During this decay, uranium disintegrates through a series of daughter products finally to radiogenic lead. The content of radiogenic lead is quite variable but can reach large values in ancient uraninite.[23,24] Lead may replace uranium to some extent and occupy interstitial sites within the uraninite structure.[25] The accumulation of lead in uraninite induces significant strain in the structure of uraninite and it is eventually released from it. Since lead is relatively immobile in most groundwaters, may form oxides or sulfurs (as galena), but also, under oxidant conditions, may precipitate in the form of uranyl containing minerals. Accumulation of radiogenic lead may also occur in the crystal structure of uranyl containing minerals leading to the destabilization of the structure and yielding the reprecipitation of lead containing secondary phases as kasolite and curite.[26,27] Kasolite may also have a non-radiogenic origin, for example from uraninite in contact with other lead containing minerals as galena under oxidant conditions.[2]

The knowledge of the structures of uranyl containing minerals has increased significantly in the last decades[2,3] due to the generation of better analytical techniques, the most important one being the introduction of charge-coupled device (CCD) detectors for X-ray diffraction.[28] These CCD detectors allow for accurate structure determinations of both small unit cell crystalline materials and of minerals with large unit cells, both types of structures being varieties frequent within the uranyl mineral groups. However, for uranyl containing materials, the resolution of the positions of the hydrogen atoms from X-ray diffraction data by structure refinement is usually not possible. Five important examples for which a full structure determination has been possible in recent times are those of the schoepite,[29] metaschoepite,[30] becquerelite[31] and curite[15] mineral phases and uranyl squarate monohydrate synthetic material (USM).[32] For schoepite, metaschoepite, becquerelite and USM, the hydrogen atom positions were successfully determined using theoretical methods. These studies are extended here since the full crystal structure of kasolite is determined in this paper using the theoretical solid-state methodology. This study confirms the full crystal structure determination, including the hydrogen atom positions, performed recently by Fejfarová *et al.*[22] While these positions may

also be obtained by using other less involved methods, as the TORQUE method,[33] which has been used recently to determine the hydrogen bond structure of curite mineral,[15] the theoretical methodology offers a more rigorous solution, since the results can be assured to be a global minimum of hypersurface of the total energy of the material in terms of the associated lattice parameters and atomic positions. Furthermore, in turn, the availability of the energy optimized full crystal structure, including the hydrogen atom positions, permits the realization of additional theoretical studies. As an example, the mechanical and Raman spectroscopic properties of kasolite are evaluated in this paper. The calculations have been carried out using first-principles theoretical solid-state methods based on density functional theory (DFT) using large plane wave basis sets and pseudopotentials for the description of internal atomic electrons.[34] At the basis of this work and a series of previous theoretical works concerning uranyl containing minerals,[29–31,33,35–47] is the seminal generation of an accurate relativistic norm conserving pseudopotential specific for uranium atom.[35,36]

This paper is organized as follows. In Section 2, the experimental and first-principles theoretical solid state methodology used in this work is described. The main results of the present paper are contained in Section 3. Section 3.1, reports the calculated crystal structure of kasolite. The hydrogen bonding structure in kasolite is discussed in Section 3.2. The computed X-ray powder pattern is reported in Section 3.3. The mechanical properties and mechanical stability of kasolite are studied in Section 3.4. The computed Raman spectrum and the assignment of the bands in this spectrum are provided in Section 3.5. In this same section the theoretical spectrum is compared with the experimental one recorded from a natural mineral sample. Finally, Section 4 presents the main conclusions of this paper.

2 Materials and methods

2.1 Experimental

The natural mineral sample studied in this work is from the Jánská vein, Příbram base metal ore district, Czech Republic.[48,49] Kasolite sample is an aggregate of lath-like to acicular crystals. This mineral sample was analyzed using Raman spectroscopy. The Raman spectrum was recorded using incident radiation perpendicular to the direction of elongation of crystals. The Raman spectrum was collected in the range 4000–45 cm^{-1} using a DXR dispersive Raman Spectrometer (Thermo Scientific) mounted on a confocal Olympus microscope. The Raman signal was excited by an unpolarised red 633 nm He–Ne gas laser and detected by a CCD detector. The experimental parameters were: 100× objective, 10 s exposure time, 100 exposures, 50 μm pinhole spectrograph aperture and 8 mW laser power level. The instrument was set up by a software-controlled calibration procedure using multiple neon emission lines (wavelength calibration), multiple polystyrene Raman bands (laser frequency calibration) and standardized white-light sources (intensity calibration). Spectral manipulations were performed using the Omnic 9 software (Thermo Scientific). The Raman spectrum was recorded for well-formed

single-crystals of kasolite. Therefore, the possibility of the presence of impurities is very small.

2.2 First-principles theoretical solid state methodology

The present theoretical study was performed using the CASTEP code,[50] a module of the Materials Studio software suite.[51] The specialized version of the Perdew–Burke–Ernzerhof energy-density functional,[52] PBEsol,[53] was used. The pseudopotentials used for H, O, Si and Pb atoms in the unit cell of kasolite mineral were standard norm-conserving pseudopotentials[54] given in CASTEP code (00PBE-OP type). The relativistic norm-conserving pseudopotential employed for uranium atom was generated from first principles in previous works.[35,36] This pseudopotential has been validated extensively in the research of uranyl containing materials.[29-31,33,35-47] The optimization of the dimensions and shape as well as the atomic positions of the unit cell of kasolite was carried out by means of the Broyden–Fletcher–Goldfarb–Shanno (BFGS) technique.[55] The plane wave kinetic energy cut-off parameter employed in the calculations was very large, $\varepsilon = 1000$ eV, and the k-mesh[56] employed was $3 \times 3 \times 2$. These parameters were chosen to obtain well converged crystal structures, energies and mechanical properties. The X-ray powder diffraction patterns were determined[57] from the optimized crystal structures using the software REFLEX implemented in the Materials Studio package.[51]

The computation of the Raman spectrum of kasolite was carried out using the linear response density functional perturbation theory (DFPT),[58-60] in the same way as in previous papers.[29,36-38,40,41,44,47,61,62] The calculated Raman shifts were not scaled to correct them for the anharmonicity and remaining approximations used in the theoretical treatment employed, such as incomplete treatment of electron correlation and basis set truncation.[63] Therefore, they correspond to the harmonic approximation of the interatomic force field.

The elastic tensor elements needed to determine the mechanical properties and to study the mechanical stability of the kasolite crystal structure were calculated from stress–strain relationships using the technique of finite deformations[64] as programmed in CASTEP code.[50] This technique has been very satisfactorily applied in the determination of the elastic response of solid materials.[29,31,33,38,39,41,44,46,65,66] The bulk modulus and its derivatives with respect to pressure were obtained by fitting the lattice volumes and associated pressures to a fourth-order Birch–Murnahan equation of state.[67] The lattice volumes in the neighborhood of the optimized equilibrium geometry were determined by optimizing the kasolite crystal structure under the effect of eighteen different applied external pressures with values in the range −1.0 to 11 GPa. EOSFIT 5.2 code[68] was used to adjust the results to the chosen equation of state. The corresponding crystal structure optimizations under pressure were also performed using the BFGS method. The three-dimensional representations of the mechanical properties of kasolite as a function of the orientation of the applied strain were performed with the ElAM software.[69]

3 Results and discussion

3.1 Crystal structure

The crystal structure of kasolite was first experimentally studied as soon as 1963 by Huynen *et al.*[19] This study was continued by a large set of subsequent studies including those of Mokeeva,[20] Rosenzweig and Ryan,[16] Stohl and Smith,[17] Vochten *et al.*,[18] Chenorukov *et al.*[21], and Fejfarová *et al.*[22] The refined structure of Fejfarová *et al.*[22] improved largely the previous proposed structures and provided the hydrogen atom positions in the kasolite unit cell. In the current study, based on density functional theory calculations, we confirmed the hydrogen bond model proposed in the work by Fejfarová *et al.*[22] The calculated atomic positions resulting from our calculations are given as ESI in an independent file of CIF (Crystallographic Information File) type.†

The crystal structure of kasolite has monoclinic symmetry, space group $P12_1/c1$ (no. 14). Table 1 gives the calculated lattice parameters, volume and density compared with the corresponding experimental information. As may be observed, the agreement is very good, the difference of the calculated volume and density with respect to the experimental values reported by Fejfarová *et al.*[22] being only about 0.9%.

Fig. 1 displays the computed crystal structure of kasolite. As may be seen in Fig. 1, U atom in kasolite is coordinated as a pentagonal bipyramid,[70] which is the most frequent coordination type among the hexavalent U structures.[71] The uranyl bipyramids share two equatorial edges to form chains expanding along b axis. As shown in the Fig. 1C, the chains are connected through silicate tetrahedra to form uranyl silicate layers perpendicular to a axis. The layers are perfectly superimposed when viewed from a direction. The silicate fragments share an edge (two oxygen atoms) with one chain and a vertex with

Table 1 Computed lattice parameters of kasolite mineral

| Parameter	a (Å)	b (Å)	c (Å)	α (deg)	β (deg)	γ (deg)	Vol. (Å^3)	Dens. (g cm^{-3})
DFT (this work)	6.7035	6.8325	13.1795	90.0	101.92	90.0	590.6266	6.605
Exp.[22]	6.705(3)	6.9257(2)	13.2857(5)	90.0	105.064(4)	90.0	595.74(3)	6.548
Exp.[16,17]	6.704	6.932	13.252	90.0	104.22	90.0	596.9788	6.535
Exp.[18]	6.7030	6.9308	13.270	90.0	104.25	90.0	597.5177	6.529
Exp.[19]	6.66	6.96	13.23	90.0	104	90.0	595.0417	6.556
Exp.[20]	6.74	6.96	13.28	90.0	104.25	90.0	603.8019	6.461
Exp.[21]	6.699	6.950	13.28	90.0	104.1	90.0	599.6630	6.505
Exp.[49]	6.716	6.924	13.256	90.0	104.17	90.0	597.6694	6.527
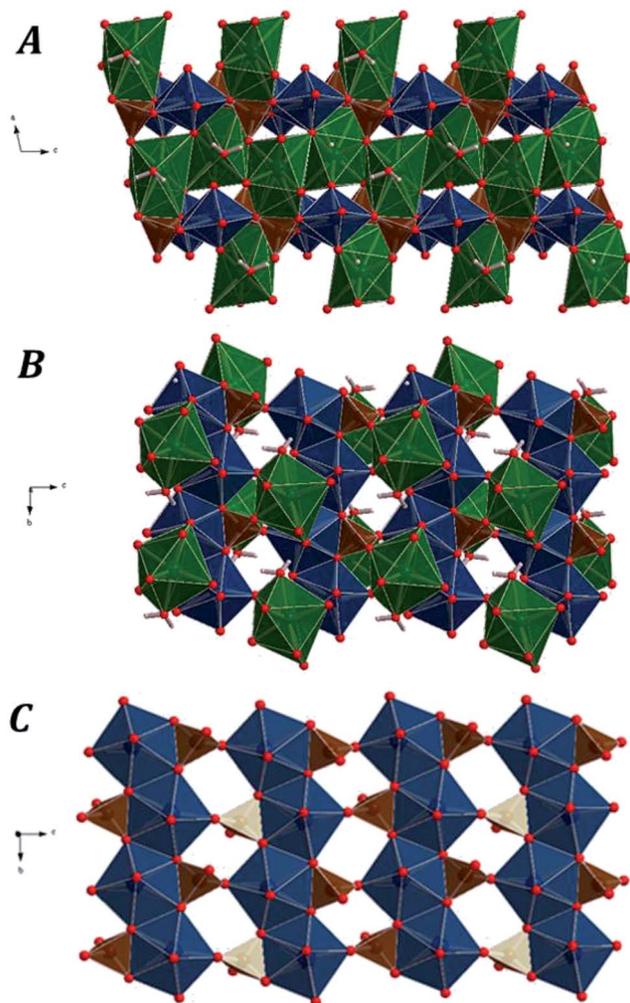
Fig. 1 Computed crystal structure of kasolite mineral: (A) view of 2 × 2 × 2 supercell from [010]; (B) view from [100]; (C) image of an isolated uranyl silicate sheet having the uranophane sheet anion-topology along [100]. Color code: U-blue; Si-brown; Pb-green; O-red; H-white.

Table 2 Interatomic distances in the crystal structure of kasolite (in Å)

Bond	Exp.[16]	Exp.[22]	Calc.
Uranyl-silicate sheet: U–O			
U–O2	1.805	1.825(7)	1.857
U–O1	1.809	1.796(6)	1.839
U–O4	2.230	2.235(5)	2.164
U–O5	2.317	2.315(5)	2.299
U–O6	2.320	2.296(5)	2.261
U–O5#	2.364	2.373(5)	2.376
U–O6#	2.543	2.550(5)	2.480
Uranyl-silicate sheet: Si–O			
Si–O3	1.588	1.603(6)	1.635
Si–O4	1.617	1.632(7)	1.630
Si–O6	1.636	1.647(5)	1.658
Si–O5	1.676	1.655(5)	1.675
Interlayer: Pb–O			
Pb–O3	2.358	2.327(5)	2.327
Pb–O3#	2.379	2.396(6)	2.374
Pb–O7w	2.540	2.529(6)	2.526
Interlayer: water			
O7w-H1	—	0.82(11)	0.978
O7w-H2	—	0.82(12)	0.997
Interlayer: hydrogen bonds (O–H···O)			
O7w···O2	—	2.962(9)	2.704
H2···O2	—	2.07(13)	1.710
O7w···O7w#	—	2.922(15)	2.988
H1···O7w#	—	2.23(14)	2.394
O7w#···Ow7	—	2.922(15)	2.988
H1···O7w	—	2.23(14)	2.394

another. The three oxygen atoms in the silicate edge and vertex from a triangle which is placed within the uranyl silicate sheet. The remaining oxygen atom in the silicate fragment points towards the interlayer space. The Pb atoms and water molecules are placed within the interlayer space. If the Pb–O bond distance cutoff is taken as 3.3 Å, the coordination number of Pb to O is eight as shown in Fig. 1. The geometric shape of the Pb coordination structure is an irregular polyhedra having 16 triangular faces, 16 edges and 8 vertices (4 equatorial vertices, 2 upper apical vertices and 2 lower apical vertices), which has a square shaped equatorial plane. As can be seen in Fig. 1, the interlayer water is not free (held to the structure by hydrogen bonding only), but structural since forms part of the lead coordination structure.

A set of representative interatomic lengths and angles are given in Tables 2 and 3 compared with the corresponding experimental values.[16,22] As can be seen, the experimental values reported by Rosenzweig and Ryan[16] were significantly improved by Fejfarová et al.[22] The values calculated in this work agree very well with the last experimental values. For example, the uranyl oxygen atoms at the apical positions of the uranyl pentagonal bipyramids have experimental[22] uranium–oxygen bond lengths (U–O1 and U–O2) of 1.796 and 1.825 Å which are in good agreement with the computed values of 1.839 and 1.857 Å, respectively. The experimental average equatorial UO distance[22] is 2.35 Å and the calculated one is 2.32 Å. These two values are close to the average value of 2.37 Å reported by Burns et al.[71] for this kind of coordination polyhedra determined from a large set of well-defined structures of uranyl containing materials.

3.2 Hydrogen bonding

There are three hydrogen bonds in the structure of kasolite. These hydrogen bonds are shown in Fig. 2. The first is a strong nearly linear bond between the water oxygen and the uranyl O2 oxygen mediated by H2. The other two are symmetry equivalent hydrogen bonds between two water molecules mediated by H1. Each pair of water molecules are hydrogen bonded by these two hydrogen bonds as shown in Fig. 2. This kind of hydrogen bonding involving two symmetrically related bonds between each pair of water molecules should be quite strong and is very interesting. As far as we are concerned, its presence has not been reported for other solid materials. Due to the large restrictions in the structural water molecule positions, imposed

Table 3 Interatomic angles in the crystal structure of kasolite (in degrees)

Angle	Exp.[16]	Exp.[22]	Calc.
Uranyl-silicate sheet: O–U–O			
O2–U–O1	175.51	176.17(19)	176.29
O1–U–O4	93.49	88.9(2)	93.17
O1–U–O5	88.80	89.9(2)	87.88
O1–U–O6	92.11	90.5(2)	92.91
O4–U–O5	78.13	91.1(2)	77.25
O4–U–O6	87.80	83.7(2)	85.70
Uranyl-silicate sheet: O–Si–O			
O3–Si–O4	115.31	114.7(3)	112.51
O3–Si–O6	113.09	113.6(3)	115.07
O3–Si–O5	108.79	107.6(3)	110.03
O4–Si–O6	112.60	113.0(3)	111.04
Interlayer: O–Pb–O			
O3–Pb–O3#	79.33	78.1(2)	77.73
O3–Pb–O7	119.85	122.74(16)	112.47
O3#–Pb–O7	70.61	71.6(3)	70.54
Interlayer: water			
H1–O7–H2	—	109.88	105.27
Interlayer: hydrogen bonds (O–H···O)			
O7–H2···O2	—	167(11)	173.98
O7–H1···O7#	—	109(10)	118.57

by the interactions with the lead central cation and the uranyl silicate sheet, the possibility of finding a similar geometrical distribution of the water molecules in other materials is very
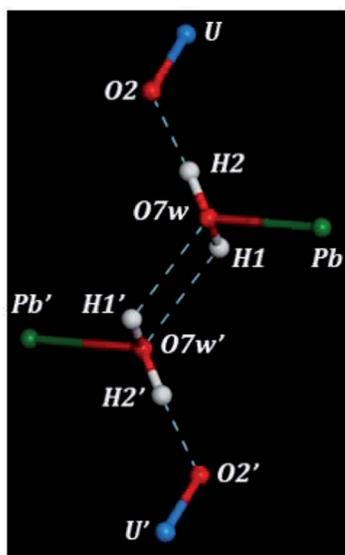

Fig. 2 Hydrogen bond structure in kasolite mineral. As may be observed, a pair of water molecules in the structure of kasolite are dually hydrogen bonded, that is, they are linked through two symmetrically related hydrogen bonds, one being directed from the first water molecule to the second one and the other from the second water molecule to the first one. Color code: U-blue; Si-brown; Pb-green; O-red; H-white.

small. Besides, the highly symmetrical and energy favored water distribution in kasolite confers to the interlayer structure a large strength and rigidity which, as shown below, is reflected in the large hardness and mechanical isotropy of kasolite structure.

3.3 X-ray powder diffraction pattern

The X-ray powder diffractograms of kasolite were determined[57] from the computed and experimental[16] crystal structures employing the software REFLEX included in Materials Studio package of programs[51] with CuK$_\alpha$ radiation ($\lambda = 1.540598$ Å). The obtained patterns are compared in Fig. 3 in which a true experimental X-ray powder diffraction pattern of kasolite[72] is also included. The agreement of the computed and experimental diffractograms is very good. This fact gives a firm support to the computed crystal structure and to the theoretical treatment used in this work.

3.4 Mechanic properties and stability

3.4.1 Elasticity matrix and mechanical stability. The symmetric stiffness matrix for a monoclinic crystalline material has 13 independent non-vanishing matrix elements.[73,74] The computed values of the C_{ij} constants are given in Table 4. The indices of the matrix elements of the elasticity matrix are expressed in this work using the standard Voigt notation in which a pair of Cartesian indices are contracted into a single integer $1 \leq i \leq 6$: $xx \rightarrow 1$, $yy \rightarrow 2$, $zz \rightarrow 3$, $yz \rightarrow 4$, $xz \rightarrow 5$, $xy \rightarrow 6$.

The generic necessary and sufficient Born criterion for stability of a monoclinic symmetry crystal structure is that all eigenvalues of the C matrix be positive.[75] Therefore, the C matrix was diagonalized numerically and all eigenvalues were found to be positive. Since the above condition was fulfilled, kasolite crystal structure is mechanically stable.

3.4.2 Mechanical properties. The elastic properties of polycrystalline kasolite aggregates were determined according to the Voigt,[76] Reuss[77] and Hill[78] schemes. The Reuss approximation, as in many previous studies,[29,31,33,38,39,44,46,65,66] was found to provide the best comparison of the results for the calculated bulk modulus, $B = 70.94 \pm 6.88$ GPa, with that determined from the equation of state (see the Section 3.4.3). The results obtained for a set of mechanical properties in the Reuss approximation are reported in Table 5. The calculated ductility index is $D = 1.51$. Hence, kasolite is a brittle material.[79,80] The calculated Vickers hardness, $H = 8.68$, corresponds to a hard material.[81] The most relevant result of those given in Table 5, is that the universal anisotropy index[82] of kasolite is very small, $A^U = 0.39$. This result was, at first sight, quite surprising due to the fact that layered materials are, in general, very anisotropic mechanically due to the fact that the bonding strength along the direction perpendicular to the structural sheets is commonly much smaller than in the remaining directions. However, the large isotropy in kasolite is easily understood at the microscopic scale in the light of the hydrogen bond structure present in the crystal structure of this mineral. Due to the strong character of the hydrogen bonding among the uranyl silicate sheets in kasolite, the bonding strength along the direction perpendicular to sheets is similar to that along the other directions.
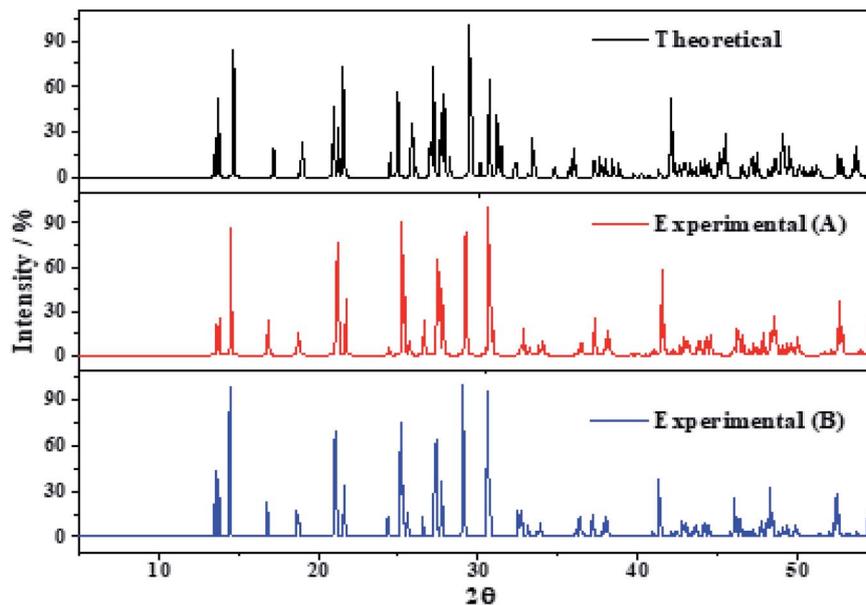
Fig. 3 X-ray diffraction powder patterns of kasolite mineral. The upper pattern has been determined from the calculated geometry. The mid pattern was obtained from the experimental geometry[16] (excluding hydrogen atom positions). Finally, the lower diffractogram is the experimental pattern of a natural mineral sample from Musonoi Extension, Shaba Province (Zaire) taken from record R060479 of the RRUFF database.[72]

In order to visualize the dependence of the mechanical properties of kasolite as a function of the direction of the applied strain in a detailed manner, the ElAM program[69] was

Table 4 Computed elastic constants of kasolite. All the values are given in GPa

ij	C_{ij}
11	108.02
22	189.96
33	165.58
44	53.02
55	40.35
66	40.08
12	45.86
13	20.05
15	−3.22
23	55.65
25	2.97
35	−0.53
46	4.24

Table 5 Computed mechanical properties of kasolite determined in the Reuss approximation[a]

Property		Value
B	Bulk modulus	70.94
G	Shear modulus	46.85
E	Young modulus	115.19
ν	Poisson ratio	0.23
D	Ductility index	1.51
H	Hardness index	8.68
A^{U}	Universal anisotropy	0.39

[a] The values of the bulk, shear and Young moduli (B, G and E) are given in GPa.

utilized to generate detailed tridimensional representations of the most important elastic properties. The results are displayed in Fig. 4. As can be observed, the Fig. 4A–D are consistent with the previous discussion about the large mechanical isotropy of this mineral. The dependence of its elastic properties with respect to the direction of the applied strain is relatively featureless in comparison with the dependence observed for other uranyl containing materials[29,31] and also non-uranyl materials.[65,66] As can be seen, this dependence is very different to that of the schoepite[29] and becquerelite,[31] despite they are also layered uranyl containing materials.

Finally, the transverse and longitudinal elastic wave velocities in kasolite were estimated using the calculated elastic constants.[44,74] The values found were $V_{L} = 4.587$ km s^{-1} and $V_{T} = 2.701$ km s^{-1} using the computed bulk and shear moduli and the calculated crystal density of 6.605 g cm^{-3} (see Table 1).
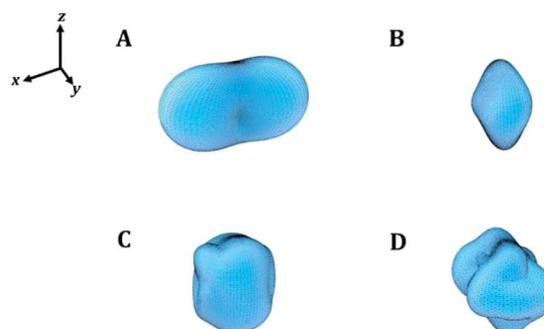

Fig. 4 Mechanical properties of kasolite mineral as a function of the orientation of the applied strain: (A) compressibility; (B) Young modulus; (C) shear modulus; (D) Poisson ratio. The maximum values of the compressibility, Young modulus, shear modulus and Poisson's ratio are 7.51 TPa^{-1}, 156.28 GPa, 59.60 GPa and 0.40, respectively.

Table 6 Computed bulk modulus and pressure derivatives of kasolite derived from the EOS[a]

Property	Value
EOS	
B (GPa)	66.08 ± 1.89
B'	2.48 ± 1.34
B'' (GPa−1)	-0.49 ± 0.29
χ^2	0.008
Elastic constants	
B (GPa)	70.94 ± 6.88

[a] The values of the bulk modulus computed from the elastic constants are also given in the last row of the table for comparison.

3.4.3 Equation of state and bulk modulus pressure derivatives. By optimizing the crystal structure of kasolite under the effect of eighteen different applied pressures, the lattice volumes near the equilibrium geometry were determined. Then, EOSFIT 5.2 code[68] was utilized to fit the calculated volume-pressure data to a fourth-order Birch–Murnaghan[67] equation of state (EOS). The fitted EOS parameters are the bulk modulus and its first two pressure derivatives. The values found are given in Table 6. As may be noticed, the calculated bulk modulus, $B = 66.08 \pm 1.89$ GPa, is in good agreement with that obtained from the elastic constants, $B = 70.94 \pm 6.88$ GPa.

3.5 Raman spectroscopy

The Raman spectra of kasolite was recorded from a natural mineral sample from the Jánská vein, Příbram base metal ore district, Czech Republic.[48,49] The resulting spectrum was compared with the theoretical spectrum computed by using density functional perturbation theory. The theoretical spectrum was computed at $T = 298$ K, $\lambda = 532$ nm, FWHM = 20 cm^{-1}. As may be seen in Fig. 5, the experimental and theoretical spectra are in very good agreement. Pictures of the atomic motions in the Raman active vibrational modes are provided in Fig. S1 of ESI.†

The analysis of the Raman spectrum was performed in four different wavenumber regions: (i) OH stretching vibration region from 3300 to 3650 cm^{-1} (Fig. 5D); (ii) H_2O bending region from 1500 to 1700 cm^{-1} (Fig. 5C); (iii) uranyl (UO_2^{2+}) and silicate (SiO_4^{4-}) fundamental vibrations region from 600 to 1100 cm^{-1} (Fig. 5B); and (iv) low wavenumber region from 45 to 600 cm^{-1} (Fig. 5A). The band wavenumbers of both spectra along with the corresponding calculated intensities and assignments are given in Table 7. The Raman band shifts and assignments performed by Frost et al.[83] are also given in this table for comparison. The Raman spectrum of Frost et al.[83] was recorded from a high purity natural specimen from El Sherana mine, South Alligator River, Northern Territory, Australia. The Raman spectrum was collected in the range between 100 and 4000 cm^{-1} at the liquid nitrogen temperature (77 K), using as
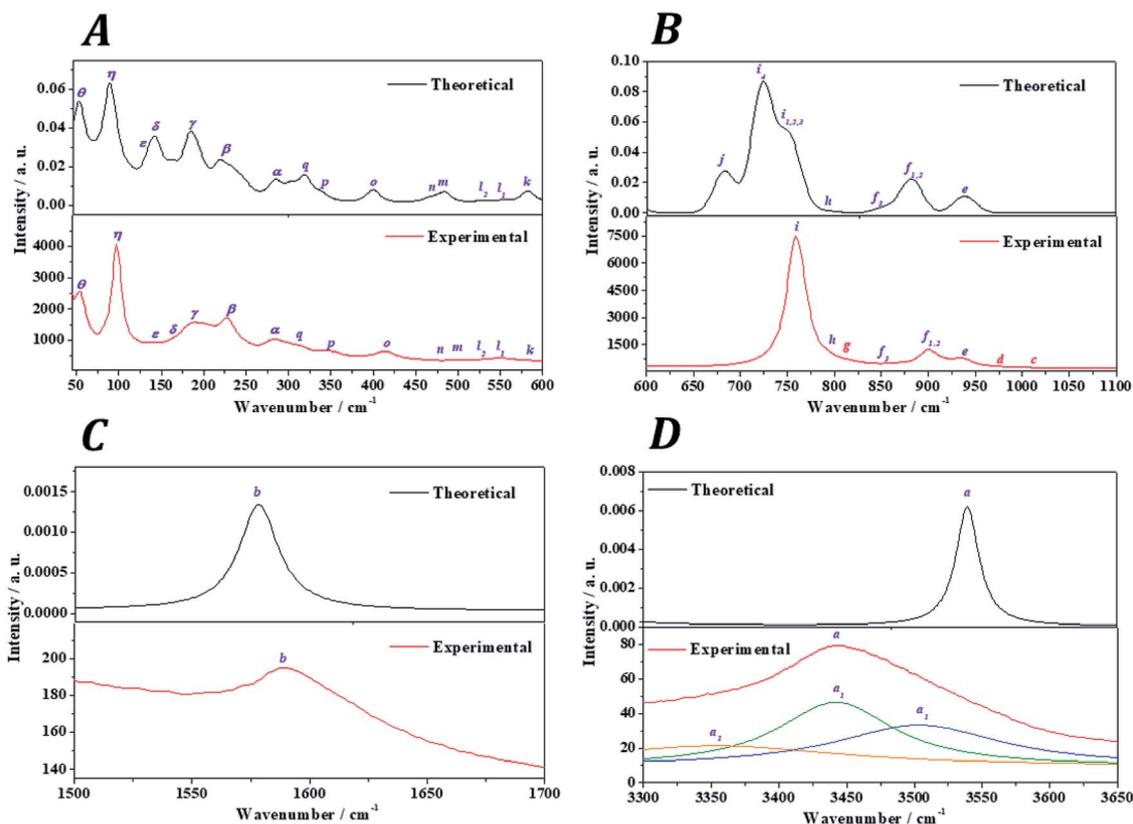

Fig. 5 Experimental and theoretical Raman spectra of kasolite mineral: (A) region: 0–600 cm^{-1}; (B) region: 600–1100 cm^{-1}; (C) region: 1500–1700 cm^{-1}; (D) region: 3300-3650 cm^{-1}.

Table 7 Experimental and calculated Raman band wavenumbers, calculated intensities and assignments of the bands in the Raman spectrum of kasolite mineral[a]

Band name	Exp. shift (cm^{-1}) [this work]	Exp. shift (cm^{-1})/assignment [Frost et al.[83]]	Calc. shift (cm^{-1})	Int. (Å^4)	Assignment [this work]
OH stretching region					
a	3503.4	$3484.2/\nu(OH)$	3555.7	12.11	$\nu(OH)$
	3441.7	$3438.2/\nu(OH)$	3540.6	174.80	$\nu(OH)$
	3354.0	$3411.1/\nu(OH)$	3540.5	1362.67	$\nu(OH)$
	3159.2	$3166.4/\nu(OH)$	3173.7	244.75	$\nu(OH)$
H2O bending region					
b	1595.3	$1593.7/\delta(HOH)$	1578.3	88.78	$\delta(HOH)$
Fundamental UO_2^{2+} and SiO_4^{4-} vibrations region					
c	1015.1	—	—	—	$\nu_1 + \nu_2 = 850.8 + 163.3 = 1014.1 \ [f_3 + \delta_1]$
					$\nu_1 + \nu_2 = 794.9 + 223.1 = 1018.0 \ [h + \beta_3]$
d	976.6	—	—	—	$\nu_1 + \nu_2 = 794.9 + 182.4 = 977.3 \ [h + \gamma_4]$
					$\nu_1 + \nu_2 = 754.4 + 223.1 = 977.5 \ [i_3 + \beta_3]$
e	936.6	$939.9/\nu^s(SiO_4^{4-})$	939.7	334.44	$\nu^s(SiO_4^{4-}) + \nu^a(UO_2^{2+})$
f	907.7	$903.6/\nu^s(SiO_4^{4-})$	883.4	660.97	$\nu^a(SiO_4^{4-})$
	900.0	$886.3/\nu^s(SiO_4^{4-})$	882.4	18.05	$\nu^a(SiO_4^{4-})$
	850.8	$876.2/\nu^a(UO_2^{2+})$	855.3	75.88	$\nu^s(SiO_4^{4-}) + l(H_2O)$
g	813.2	$820.8/\nu^a(UO_2^{2+})$	—	—	$\nu_1 + \nu_2 = 759.2 + 55.1 = 814.3 \ [i_2 + \theta]$
					$\nu_1 + \nu_2 = 713.9 + 102.6 = 816.5 \ [i_4 + \eta_1]$
					$\nu_1 + \nu_2 = 529.7 + 283.8 = 813.5 \ [l_2 + \alpha_1]$
h	794.9	$793.9/\nu^s(UO_2^{2+})$	793.1	32.11	$\nu^a(SiO_4^{4-})$
i	767.9	$766.7/\nu^s(UO_2^{2+})$	762.8	132.53	$\nu(UO_2^{2+}) + l(H_2O)$
	759.2	$758.7/\nu^s(UO_2^{2+})$	750.2	295.86	$\nu(UO_2^{2+}) + l(H_2O)$
	754.4	$750.0/\nu^s(UO_2^{2+})$	750.4	794.50	$\nu(UO_2^{2+}) + l(H_2O)$
	713.9	$721.3/\nu^s(UO_2^{2+})$	723.3	1870.19	$\nu(UO_2^{2+}) + l(H_2O)$
j	—	—	683.2	557.03	$l(H_2O)$
Low wavenumber region					
k	574.3	$575.9/\delta(SiO_4^{4-}) \ [\nu_2]$	583.5	100.66	$l(H_2O)$
l	549.0	$550.4/\delta(SiO_4^{4-}) \ [\nu_2]$	554.2	23.53	$\nu(UO_2^{2+}) + \nu(UO_{eq}) + \gamma(SiO_4^{4-}) + l(H_2O)$
	529.7	$533.3/\delta(SiO_4^{4-}) \ [\nu_2]$	529.5	17.81	$\nu(UO_{eq}) + \gamma(SiO_4^{4-}) + l(H_2O)$
m	502.7	$501.1/\delta(SiO_4^{4-}) \ [\nu_2]$	485.0	75.81	$l(H_2O)$
n	457.4	$454.6/\delta(SiO_4^{4-}) \ [\nu_2]$	467.2	19.21	$l(H_2O)$
o	414.0	$415.1/\delta(SiO_4^{4-}) \ [\nu_2]$	400.8	80.21	$\delta(OSiO) + l(H_2O)$
p	347.9	341.4	339.3	28.03	$\rho(UO_2^{2+}) + w(OUO_{eq}) + t(OUO_{eq}) + \gamma(SiO_4^{4-}) + l(H_2O)$
q	316.2	319.0	319.7	71.01	$\rho(UO_2^{2+}) + w(OUO_{eq}) + t(OUO_{eq}) + \gamma(SiO_4^{4-}) + l(H_2O)$
r	293.5	302.5	303.1	37.50	$\delta(UO_2^{2+}) + \delta^{op}(UO_{eq}) + \gamma(SiO_4^{4-}) + T(H_2O)$
α	283.8	285.3	285.9	30.52	$\rho(UO_2^{2+}) + w(OUO_{eq}) + t(OUO_{eq}) + \gamma(SiO_4^{4-}) + l(H_2O)$
	277.1		283.4	25.04	$\delta(UO_2^{2+}) + t(OUO_{eq}) + l(H_2O)$
β	234.7	234.3	246.3	29.01	$\rho(UO_2^{2+}) + w(OUO_{eq}) + l(H_2O)$
	228.9	231.1	232.9	37.18	$\gamma(UO_2^{2+}) + t(SiO_4^{4-}) + T(H_2O)$
	223.1	217.7	221.0	33.37	$\gamma(UO_2^{2+}) + T(H_2O)$
γ	202.8	184.7	197.9	24.78	$\rho(UO_2^{2+}) + \delta(UOSi) + T(H_2O)$
	192.2		191.6	37.87	$\gamma(UO_2^{2+}) + \delta(UOSi) + T(H_2O)$
	187.4		185.3	38.35	$\rho(UO_2^{2+}) + w(OUO_{eq}) + t(OUO_{eq}) + \gamma(SiO_4^{4-}) + T(H_2O)$
	182.4		182.9	40.54	$\rho(UO_2^{2+}) + T(H_2O)$
δ	163.3	165.3	146.1	25.13	$\rho(UO_2^{2+}) + \delta^{op}(UO_{eq}) + T(H_2O)$
	155.6	153.5	143.8	19.28	$T(H_2O)$
ε	143.1	140.1	138.3	22.31	$\rho(UO_2^{2+}) + \delta^{op}(UO_{eq}) + T(H_2O)$
η	102.6	107.5	108.7	3.14	$\nu(PbO) + T(UO_2^{2+}) + T(SiO) + T(H_2O)$
	97.7	99.6	90.6	52.12	$\nu(PbO) + T(UO_2^{2+}) + T(SiO) + T(H_2O)$
θ	55.1	—	53.6	9.61	$\nu(PbO) + \gamma(UO_2^{2+}) + T(H_2O)$

[a] Raman shifts and assignments performed by Frost et al.[83] are also given for comparison.

excitation source a HeNe laser (633 nm). The spectral resolution achieved was 2 cm^{-1}.

(i) OH stretching vibrations region: the experimental and theoretical Raman spectra of the hydroxyl stretching region are shown in Fig. 5D. The experimental spectrum displays a wide band having three main components located at 3503, 3442 and 3365 cm^{-1}. A fourth very broad component is placed at 3159 cm^{-1}. Frost et al.[83] found these components at 3484, 3438, 3411 and 3166 cm^{-1}, respectively. These components are reproduced theoretically at 3556, 3541, 3540 and 3174 cm^{-1}.

(ii) H_2O bending region: the experimental and theoretical spectra of this region are shown in Fig. 5C. The experimental spectrum displays a single band at 1595 cm^{-1} (found by Frost *et al.*[83] at 1594 cm^{-1}). This band corresponds to the theoretical water molecule bending band located at 1578 cm^{-1}.

(iii) Uranyl (UO_2^{2+}) and silicate (SiO_4^{4-}) fundamental vibrations region: the experimental spectrum of this region presents two first weak bands, referred to as c and d, respectively, in Table 7 located at 1015 and 977 cm^{-1}. These bands were not detected by Frost *et al.*[83] and are absent in the theoretical spectrum. These two bands are identified as combination bands as indicated in Table 7. The third band located at 937 cm^{-1} is satisfactorily reproduced by the theoretical calculations at 940 cm^{-1}. This band was assigned by Frost *et al.*[83] to silicate symmetric stretching vibrations, $\nu^s(SiO_4^{4-})$. This assignment is confirmed here. However, as may be seen in Table 7, this band contain also significant contributions from uranyl antisymmetric stretching vibrations (see Fig. S1 of the ESI†). The next bands at 908 and 900 cm^{-1}, correspond to the bands calculated at 883 and 882 cm^{-1} and are assigned to silicate asymmetric stretching vibrations, $\nu^a(SiO_4^{4-})$. The term asymmetric is used instead of antisymmetric because the silicate symmetry is lost in these vibrations. In this case the assignment performed by Frost *et al.*[83] seems to be incorrect since, as the 937 cm^{-1} band, these bands were attributed to silicate symmetric stretching vibrations. The experimental band placed at 851 cm^{-1} is reproduced at 855 cm^{-1} and is ascribed to a combination of silicate symmetric stretching vibrations and water librations. Again, Frost *et al.*[83] assigned this band differently to uranyl antisymmetric stretching vibrations, which, as has been noticed, appear at higher wavenumbers.

The weak band called g and placed at 813 cm^{-1} (found at 821 cm^{-1} by Frost *et al.*[83]), does not appear in the theoretical Raman spectrum and, as the bands c and d, is identified as a combination band. This identification was not recognized by Frost *et al.*[83] which attributed this band to uranyl antisymmetric stretching vibrations. The set of five experimental bands at 795, 768, 759, 754 and 714 cm^{-1} correspond to the theoretical bands placed at 793, 763, 750, 750 and 723 cm^{-1}. All these bands were assigned by Frost *et al.*[83] to the fundamental uranyl symmetric stretching vibrations, $\nu^s(UO_2^{2+})$. In the present work, the assignment is the same for the last four bands. However, the first band is attributed to silicate asymmetric stretching vibrations. The band calculated at 683 cm^{-1}, ascribed to water librations, is not observed in the present experimental spectrum and in that from Frost *et al.*[83]

(iv) Low wavenumber region: the first six bands in this spectral region observed at 574, 549, 530, 503, 457 and 414 cm^{-1} are very well reproduced theoretically at 583, 554, 529, 485, 467 and 401 cm^{-1}. The first four of these bands were assigned by Frost *et al.*[83] to ν_2 silicate bending modes and the last two bands to ν_4 silicate bending modes.[84] This assignment is not supported by this study. The symmetry of these vibrations is lost in kasolite. According to the normal mode analysis of the theoretical spectrum, the bands located at 574, 503 and 457 cm^{-1} should be attributed to water librations only. Similarly, the band placed at 549 cm^{-1} is ascribed to a combination of uranyl

and equatorial UO stretching vibrations, silicate deformations and water librations. The band at 530 cm^{-1} is assigned to a combination of equatorial UO stretching vibrations, silicate deformations and water librations. Finally, the band at 414 cm^{-1} is assigned to OSiO bending vibrations and water librations.

The bands at 348, 316, 294, 284, 277, 235, 229 and 223 correspond to the calculated bands at 339, 320, 303, 286, 283, 246, 233 and 221 cm^{-1}. The whole set was assigned to uranyl bending vibrations by Frost *et al.*[83] Again, this assignment is not supported by the theoretical work. The assignment of these bands is complicated and is given in detail in Table 7. As may be observed, the interpretation of the origin of these bands involves a large series of atomic motions as the uranyl bending, $\delta(UO_2^{2+})$, the uranyl rotation, $\rho(UO_2^{2+})$, and the uranyl deformation, $\gamma(UO_2^{2+})$, motions. The difference between these three kinds of uranyl atomic motions is illustrated in Fig. 6. As can be seen, the bending and rotation motions involve displacements of the uranyl oxygens out of the uranyl axis in the same and opposite directions. In the deformation motion, each oxygen displaces in a different direction. Since the uranyl fragment displays these three different types of motion, this spectral region should not be referred to as uranyl bending region. Other types of motions involving atomic motions in the uranyl polyhedra are the equatorial OUO wagging and twisting vibrations, $w(OUO_{eq})$ and $t(OUO_{eq})$ and the equatorial out of plane UO bending vibration, which are also shown in Fig. 6.

Finally, the good agreement obtained for the positions of the experimental bands at very low wavenumbers, 203, 192, 187, 182, 163, 156, 143, 103, 98 and 55 cm^{-1}, with those determined theoretically (198, 192, 185, 183, 146, 144, 138, 109, 91 and 54 cm^{-1}) is a very satisfactory feature due to the great difficulty of reproducing these types of bands using first-principles methods. In general, it is impossible to assign the bands of very low wavenumbers empirically and they are simply ascribed without any specification to deformation, translational and rotational motions. The excellent agreement obtained allowed
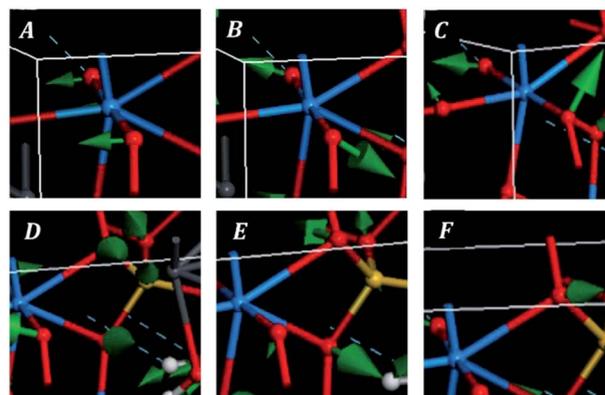

Fig. 6 Images of selected atomic motions in the vibrational normal modes of the low wavenumber region of kasolite mineral: (A) uranyl bending; (B) uranyl rotation; (C) uranyl deformation; (D) equatorial OUO wagging; (E) equatorial OUO twisting; (F) equatorial out of plane UO bending.
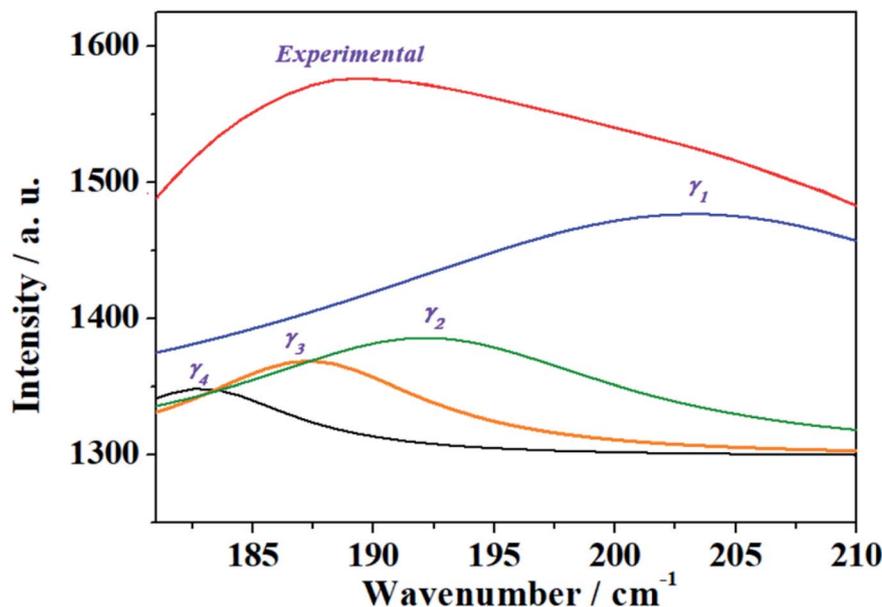
Fig. 7 Resolution into single band contributions of the band γ in the experimental Raman spectrum of kasolite mineral.

to assign all these bands, providing a detailed description of the origin of these bands (see Table 7).

3.5.1   Resolution of Raman bands into components. One of the first tasks to be performed when an experimental vibrational (Raman or infrared) spectrum is recorded is the resolution of the bands into components. This is due to the broadening and overlap of the single bands which do not allow for a simple resolution. This task is usually performed using Lorentzian fits, which is quite difficult because several possible resolutions are frequently possible using different numbers of components and initial locations of the associated peaks. Only one of these possibilities corresponds to the physical reality and several resolutions may lead to reasonable fitting statistics. If an incorrect selection is made, the results will be unphysical. This problem could be minimized if accurate quantum theoretical computations are carried out because their results provide the number of single components and their approximate positions. The case of kasolite is specially complicated because, as can be seen in Table 7, a large series of experimental bands require resolution. The resolution of the experimental kasolite Raman bands into components using the number of components and initial positions obtained in the theoretical computations is illustrated in Fig. 7 and S2 of the ESI.† Despite of this difficulty, the resolution into components performed in the work by Frost *et al.*[83] is excellent, leading in most cases to the correct number of bands and locations. However, the resolution of band γ was not performed and this band was left as a single component. The theoretical calculations revealed the existence of four Raman allowed vibrational transitions with associated wavenumbers close to 185 cm^{-1} (see Fig. 7). The resolution of this band yielded the position of four sub-bands with wavenumbers 203, 192, 187 and 182 cm^{-1}. Consequently, theoretical calculations are a very useful tool to reduce the ambiguity and complexity of resolving and assigning the experimental vibrational spectra.

4   Conclusions

The crystal structure of kasolite mineral was obtained by using first-principles theoretical solid-state methods. The structure optimization was carried out by employing the PBEsol exchange–correlation energy-density functional. The computed structure confirmed the experimental observations[22] since the lattice parameters, interatomic distances and angles, and X-ray powder pattern were in good agreement with the experimental information. The detailed analysis of the hydrogen bond structure revealed that the hydrogen bonding in kasolite is strong and dual. The water molecules in kasolite are distributed in pairs held together by two symmetrically related hydrogen bonds (one being directed from the first water molecule to the second one and the other from the second water molecule to the first one). The availability of the energy optimized hydrogen atom positions in kasolite permitted the theoretical computation of its mechanical properties and Raman spectrum because the application of the theoretical methodology for their calculation requires the knowledge of the optimized full crystal structure.

From the calculated elasticity matrix, the mechanical stability of the kasolite crystal structure was studied and a large series of relevant mechanical data was obtained. The computed mechanical properties include the bulk modulus and its pressure derivatives, the Young and shear moduli, the Poisson ratio and the ductility, hardness and anisotropy indices. Since these properties have not been measured experimentally, their values were predicted. Kasolite is shown to be a hard and brittle mineral having a large bulk modulus of the order of B $\sim$71 GPa. Kasolite has a great mechanical isotropy despite of being a layered material. This property is the direct consequence of the strong hydrogen bonding between the structural uranyl silicate sheets in kasolite, which makes the bonding strength along the direction perpendicular to the layers of similar magnitude to that along the remaining directions.

Finally, the Raman spectrum of a natural sample of kasolite was recorded and compared with the computed Raman spectrum. Since the agreement was very good, the theoretical calculations were used to assign the bands of the experimental spectrum. A large number of kasolite Raman bands were reassigned. Three bands of the experimental spectrum, located at the wavenumbers 1015, 977 and 813 cm^{-1}, were identified as combination bands. The theoretical calculations were also found to be an extremely useful tool to guide the resolution into single components of the bands of the experimental spectrum.

Conflicts of interest

There are no conflicts to declare.

Acknowledgements

References

1 A. Schoep, *C. R. Acad. Sci.*, 1922, **173**, 1476–1477.
2 S. V. Krivovichev, J. Plášil, in *Uranium: From Cradle to Grave*, ed. P. C. Burns, G. E. Sigmon, Mineralogical Association of Canada Short Courses, 2013, vol. 43, pp. 15–119.
3 R. J. Finch and T. Murakami, *Rev. Mineral. Geochem.*, 1999, **38**, 91–180.
4 C. Frondel, *Am. Mineral.*, 1956, **41**, 539–568.
5 R. M. Garrels and C. L. Christ, *U.S. Geol. Surv. Prof. Pap.*, 1959, **320**, 81–89.
6 R. J. Finch and R. C. Ewing, *J. Nucl. Mater.*, 1992, **190**, 133–156.
7 I. Grenthe, J. Drozdzynski, T. Fujino, E. C. Buck, T. E. Albrecht-Schmitt and S. F. Wolf, in *The Chemistry of Actinide and Transactinide Elements*, ed. L. R. Morss, N. M. Edelstein and J. Fuger, Springer Science and Business Media, Berlin, 2006, ch V, vol. I, pp. 253–638.
8 J. Plášil, *J. Geosci.*, 2014, **59**, 99–114.
9 R. J. Finch and R. C. Ewing, *SKB Technical Report 91-15*, SKB, Stockholm, 1991.
10 R. S. Forsyth and L. O. Werme, *J. Nucl. Mater.*, 1992, **190**, 3–19.
11 E. C. Pearcy, J. D. Prikryl, W. M. Murphy and B. W. Leslie, *Appl. Geochem.*, 1994, **9**, 713–732.
12 D. J. Wronkiewicz, J. K. Bates, T. J. Gerding, E. Veleckis and B. S. Tani, *J. Nucl. Mater.*, 1992, **190**, 107–127.
13 D. J. Wronkiewicz, J. K. Bates, S. F. Wolf and E. C. Buck, *J. Nucl. Mater.*, 1996, **238**, 78–95.
14 P. C. Burns, *Am. Mineral.*, 1997, **82**, 1176–1186.
15 S. Ghazisaeed, B. Kiefer and J. Plášil, *RSC Adv.*, 2019, **9**, 10058–10063.
16 A. Rosenzweig and R. R. Ryan, *Cryst. Struct. Commun.*, 1977, **6**, 617–621.
17 F. V. Stohl and D. K. Smith, *Am. Mineral.*, 1981, **66**, 610–625.
18 R. Vochten, N. Blaton, O. Peeters, k. Van Springel and L. Van Haverbeke, *Can. Mineral.*, 1997, **35**, 735–741.
19 A. M. Huynen, J. Piret-Meunier and M. Van Meerssche, *Acad. R. Belg., Bull.*, 1963, **49**, 192–201.
20 V. I. Mokeeva, *Sov. Phys. Crystallogr.*, 1965, **9**, 621–622.
21 N. G. Chernorukov, A. V. Knyazev and O. V. Nipruk, *Radiochem*, 2007, **49**, 340–345.
22 K. Fejfarová, M. Dušek, J. Plášil, J. Čejka, J. Sejkora and R. Škoda, *J. Nucl. Mater.*, 2013, **434**, 461–467.
23 R. M. Berman, *Am. Mineral.*, 1957, **42**, 705–731.
24 J. Janeczek and R. C. Ewing, *Geochim. Cosmochim. Acta*, 1995, **59**, 1917–1931.
25 J. Janeczek and R. C. Ewing, *J. Nucl. Mater.*, 1992, **190**, 128–132.
26 H. Isobe, T. Murakami and R. C. Ewing, *J. Nucl. Mater.*, 1992, **190**, 174–187.
27 R. J. Finch and R. C. Ewing, *Am. Mineral.*, 1997, **82**, 607–619.
28 P. C. Burns, *Can. Mineral.*, 1998, **36**, 847–853.
29 F. Colmenero, J. Cobos and V. Timón, *Inorg. Chem.*, 2018, **57**, 4470–4481.
30 F. Colmenero, A. M. Fernández, J. Cobos and V. Timón, *ACS Earth Space Chem.*, 2019, **3**, 17–28.
31 F. Colmenero, A. M. Fernández, J. Cobos and V. Timón, *RSC Adv.*, 2019, **8**, 24599–24616.
32 F. Colmenero, J. Cobos and V. Timón, *J. Phys.: Condens. Matter*, 2019, **31**, 175701.
33 S. Ghazisaeed, J. Majzlan, J. Plášil and B. Kiefer, *J. Appl. Crystallogr.*, 2018, **51**, 1116–1124.
34 M. C. Payne, M. P. Teter, D. C. Ailan, A. Arias and J. D. Joannopoulos, *Rev. Mod. Phys.*, 1992, **64**, 1045–1097.
35 F. Colmenero, PhD thesis, Universidad Autónoma de Madrid, Madrid, 2017, p. 443.
36 L. J. Bonales, F. Colmenero, J. Cobos and V. Timón, *Phys. Chem. Chem. Phys.*, 2016, **18**, 16575–16584.
37 F. Colmenero, L. J. Bonales, J. Cobos and V. Timón, *Spectrochim. Acta, Part A*, 2017, **174**, 245–253.
38 F. Colmenero, L. J. Bonales, J. Cobos and V. Timón, *J. Solid State Chem.*, 2017, **253**, 249–257.
39 F. Colmenero, L. J. Bonales, J. Cobos and V. Timón, *J. Phys. Chem. C*, 2017, **121**, 5994–6001.
40 F. Colmenero, L. J. Bonales, J. Cobos and V. Timón, *J. Phys. Chem. C*, 2017, **121**, 14507–14516.
41 F. Colmenero, L. J. Bonales, J. Cobos and V. Timón, *Clay Miner.*, 2018, **53**, 377–392.
42 F. Colmenero, A. M. Fernández, J. Cobos and V. Timón, *J. Phys. Chem. C*, 2018, **122**, 5254–5267.

43 F. Colmenero, A. M. Fernández, J. Cobos and V. Timón, *J. Phys. Chem. C*, 2018, **122**, 5268–5279.

44 F. Colmenero, in *Minerals*, ed. K. S. Essa, InTechOpen, London, 2018, ISBN: 978-953-51-6784-6.

45 F. Colmenero, in *Density Functional Theory*, ed. D. Glossman-Mitnik, InTechOpen, London, 2018, ISBN: 978-953-51-7020-4.

46 F. Colmenero, *Appl. Sci.*, 2018, **8**, 2281–2290.

47 F. Colmenero, J. Cobos and V. Timón, *Theor. Chem. Acc.*, 2019, **138**, 43.

48 P. Škácha, V. Goliáš, J. Sejkora, J. Plášil, L. Strnad, R. Škoda and J. Ježek, *J. Geosci.*, 2009, **54**, 1–13.

49 J. Sejkora, J. Litochleb, J. Čejka and P. Černý, *Bull. Mineral.-Petrolog. Odd. Nár. Muz.*, 2013, **21**, 37–46.

50 S. J. Clark, M. D. Segall, C. J. Pickard, P. J. Hasnip, M. I. J. Probert, K. Refson and M. C. Payne, *Z. Kristallogr.*, 2005, **220**, 567–570.

51 *MaterialsStudio*, http://3dsbiovia.com/products/collaborativescience/biovia-materials-studio/, accessed April 1, 2019.

52 J. P. Perdew, K. Burke and M. Ernzerhof, *Phys. Rev. Lett.*, 1996, **77**, 3865–3868.

53 J. P. Perdew, A. Ruzsinszky, G. I. Csonka, O. A. Vydrov, G. E. Scuseria, L. A. Constantin, X. Zhou and K. Burke, *Phys. Rev. Lett.*, 2008, **100**, 136406.

54 N. Troullier and J. L. Martins, *Phys. Rev. B: Condens. Matter Mater. Phys.*, 1991, **43**, 1993–2006.

55 B. G. Pfrommer, M. Cote, S. G. Louie and M. L. Cohen, *J. Comput. Phys.*, 1997, **131**, 233–240.

56 H. J. Monkhorst and J. D. Pack, *Phys. Rev. B: Condens. Matter Mater. Phys.*, 1976, **13**, 5188–5192.

57 R. T. Downs, K. L. Bartelmehs, G. V. Gibbs and M. B. Boisen, *Am. Mineral.*, 1993, **78**, 1104.

58 S. Baroni, S. de Gironcoli and A. Dal Corso, *Rev. Mod. Phys.*, 2001, **73**, 515–562.

59 C. Lee and X. Gonze, *Phys. Rev. B: Condens. Matter Mater. Phys.*, 1995, **51**, 8610–8613.

60 K. Refson, P. R. Tulip and S. J. Clark, *Phys. Rev. B: Condens. Matter Mater. Phys.*, 2006, **73**, 155114.

61 F. Colmenero and V. Timon, *J. Solid State Chem.*, 2018, **263**, 131–140.

62 F. Colmenero, *J. Phys. Chem. Solids*, 2019, **125**, 31–42.

63 W. J. Hehre, L. Radom, P. V. R. Schleyer and J. A. Pople, *Ab Initio Molecular Orbital Theory*, Wiley, New York, 1986.

64 R. Yu, J. Zhu and H. Q. Ye, *Comput. Phys. Commun.*, 2010, **181**, 671–675.

65 F. Colmenero, *Mater. Res. Express*, 2019, **6**, 045610.

66 F. Colmenero, *Phys. Chem. Chem. Phys.*, 2019, **21**, 2673–2690.

67 F. Birch, *Phys. Rev.*, 1947, **71**, 809–824.

68 (*a*) R. J. Angel, *Rev. Mineral. Geochem.*, 2000, **41**, 35–60; (*b*) *EOSFIT 5.2 software*, http://www.ccp14.ac.uk/ccp/web-mirrors/ross-angel/rja/soft/, accessed April 1, 2019.

69 A. Marmier, Z. A. D. Lethbridge, R. Walton, C. W. Smith, S. C. Parker and K. E. Evans, *Comput. Phys. Commun.*, 2010, **181**, 2102–2115.

70 H. T. Evans, *Science*, 1963, **141**, 154–158.

71 P. C. Burns, R. C. Ewing and F. C. Hawthorne, *Can. Mineral.*, 1997, **35**, 1551–1570.

72 R. T. Downs, *Abstracts of the 19th General Meeting of the International Mineralogical Association in Kobe*, Japan, 2006, O03-13; RRUFF database, http://rruff.info/kasolite, Record RRUFF-060479.

73 J. F. Nye, *The Physical Properties of Crystals: Their Representation by Tensors and Matrices*, Oxford University Press, New York, 1985.

74 P. F. Weck, E. Kim and E. C. Buck, *RSC Adv.*, 2015, **5**, 79090–79097.

75 F. Mouhat and F.-X. Coudert, *Phys. Rev. B: Condens. Matter Mater. Phys.*, 2014, **90**, 224104.

76 W. Voigt, *Lehrbuch der Kristallphysik*, Teubner, Leipzig, 1962.

77 A. Reuss, *Z. Angew. Math. Mech.*, 1929, **9**, 49–58.

78 R. Hill, *Proc. Phys. Soc., London*, 1952, **65**, 349–354.

79 S. F. Pugh, *Philos. Mag.*, 1954, **45**, 823–843.

80 Y. Bouhadda, S. Djella, M. Bououdina, N. Fenineche and Y. Boudouma, *J. Alloys Compd.*, 2012, **534**, 20–24.

81 H. Niu, P. Wei, Y. Sun, C.-X. Chen, C. Franchini, D. Li and Y. Li, *Appl. Phys. Lett.*, 2011, **99**, 031901.

82 S. I. Ranganathan and M. Ostoja-Starzewski, *Phys. Rev. Lett.*, 2008, **101**, 055504.

83 R. L. Frost, J. Čejka, M. L. Weier and W. Martens, *J. Raman Spectrosc.*, 2006, **37**, 538–551.

84 K. Nakamoto, *Infrared and Raman Spectra of Inorganic and Coordination Compounds*, J. Wiley and Sons, New York, 1986.